Volume 27
Number 44
28 November 2025
Pages 23501–24114

PCCP

Physical Chemistry Chemical Physics

rsc.li/pccp

25 YEARS ANNIVERSARY

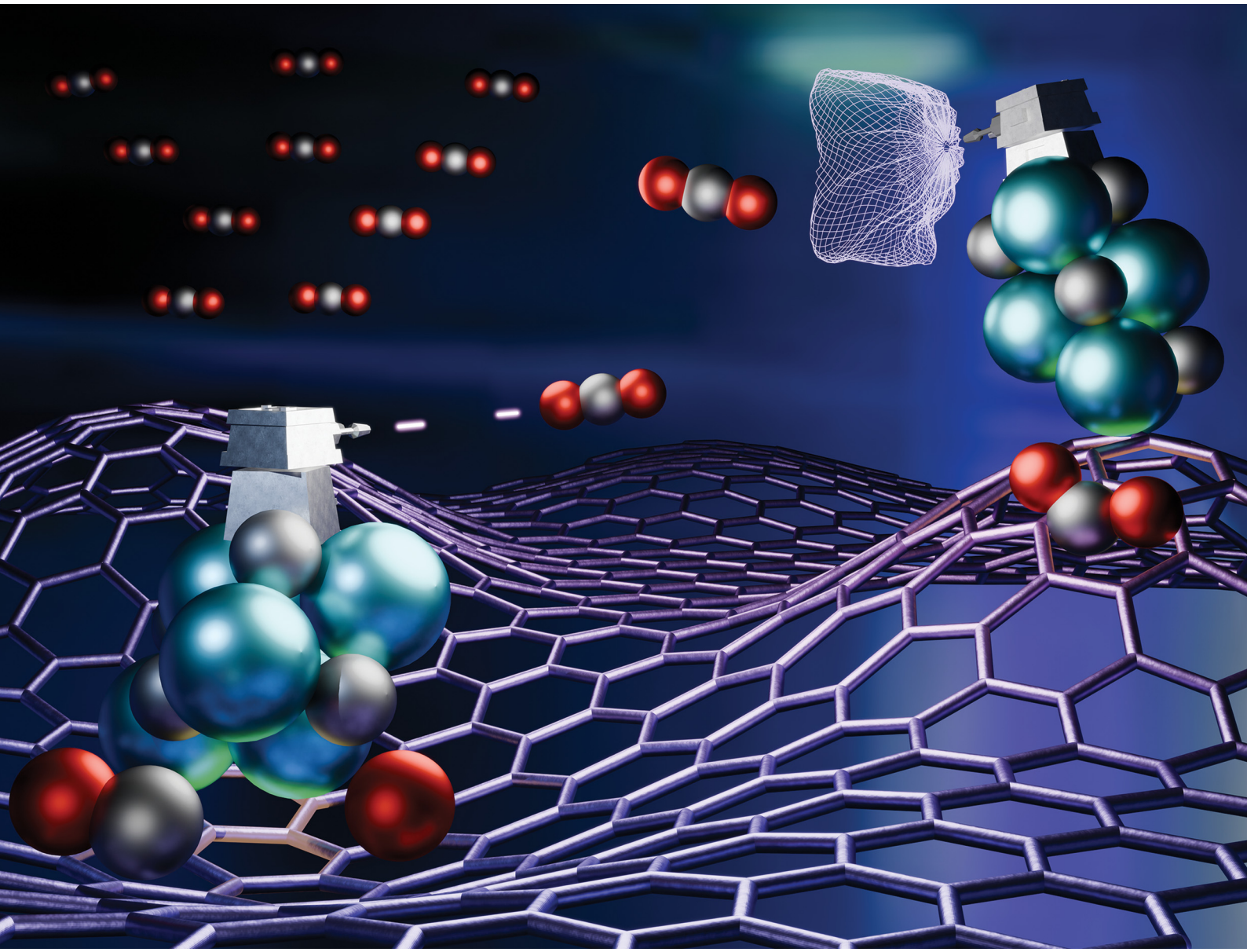

ISSN 1463-9076

ROYAL SOCIETY OF CHEMISTRY

PAPER

Francesc Illas *et al.*

Carbon support curvature modulates CO_2 activation on molybdenum carbide clusters

PCCP Owner Societies

PCCP

PAPER

View Article Online
View Journal | View Issue

Cite this: *Phys. Chem. Chem. Phys.*, 2025, **27**, 23561

Carbon support curvature modulates CO_2 activation on molybdenum carbide clusters

Wei Cao, Francesc Viñes and Francesc Illas *

Received 16th July 2025,
Accepted 11th September 2025

DOI: 10.1039/d5cp02714d

rsc.li/pccp

Density functional theory (DFT) is employed to investigate CO_2 adsorption and activation on a representative Mo_6C_5 cluster supported on both flat and curved graphene, with particular focus on the effects of support curvature. In the free-standing cluster, a locally metal-rich triangular Mo_3 site exhibits the strongest CO_2 binding. However, this highly reactive site anchors to the carbon support, thus becoming inaccessible to adsorbates, simultaneously conferring enhanced CO_2 activation capability to the remaining stoichiometric Mo–C sites. Support curvature provides an additional lever: MoC_y clusters in convex regions further strengthen CO_2 adsorption, whereas those in concave regions thermodynamically and kinetically favor CO_2 dissociation, thereby facilitating subsequent conversion steps. These findings reveal the dual structural and electronic roles of carbon supports, paving the way for designing more tailor-made MoC_y/C-based catalysts for CO_2 utilization.

1. Introduction

The increasing concentration of atmospheric carbon dioxide (CO_2) has resulted in the critical environmental problem of global warming, highlighting the need for efficient strategies to capture and convert it into value-added chemicals.[1,2] However, the intrinsic stability of CO_2 makes its activation and subsequent conversion a true obstacle.[3,4] Recently, noble transition metals such as gold (Au),[5] platinum (Pt),[6] and palladium (Pd)[7] have been demonstrated as capable of CO_2 activation and conversion, *e.g.*, through hydrogenation or reduction through the reverse water–gas shift (RWGS) reaction. However, the scarcity and associated high cost of these metals underline the need and urgency to find other sustainable and earth-abundant alternatives.[8]

Transition metal carbides (TMCs) have attracted research attention over recent decades as promising, economic substitute catalysts for Pt-group metals, with enhanced poison resistances, catalytic activities, or selectivities.[9–11] Among all possible TMCs, molybdenum carbides (MoC and Mo_2C) stand out, both as catalysts themselves,[12] and as supports[13] for metal clusters, which exhibit notable activity in key CO_2 conversion reactions, including CO_2 hydrogenation,[14] the RWGS,[15] or the electrochemical CO_2 reduction,[16,17] to name a few.

As observed in polycrystalline MoC catalyst samples, extended surfaces with different Miller indices exhibit distinct reactivities toward CO_2 conversion. For example, on the orthorhombic β-Mo_2C (001) polar surface, CO_2 can spontaneously dissociate into CO* and O* on the Mo-terminated surface. In contrast, on the C-terminated facet, the molecule is activated but tends to retain its C═O bonds.[18] Furthermore, when studying RWGS over the hexagonal α-Mo_2C phase,[12] surface orientation has been shown to significantly influence catalytic performance. Specifically, the (201)-Mo/C, (001)-Mo, and (001)-C surfaces bind the adsorbate too strongly, thereby hindering the release of reaction products. In comparison, the (101)-Mo/C surface shows a better balance among CO_2 activation, dissociation, and desorption of surface intermediates. This finding integrates theoretical reaction energy profiles, which indicate that this surface is preferentially expressed on high-temperature Mo_2C nanoparticles.[19] All these studies underscore the critical role of surface structure in determining CO_2 activation and conversion behavior.

Recent advances in controlled catalyst synthesis have enabled the preparation of well-defined MoC nanoparticles, referred to as MoC_y NPs.[20] These nanostructured catalysts have been shown to feature an improved catalytic performance compared to single-crystal surfaces and bulk powders.[21] By controlling the size at the nanometer or sub-nanometer scale and adjusting MoC_y stoichiometry, the catalytic activity towards CO_2 can be tuned. For example, Mo-rich $MoC_{0.6}$ NPs supported on Au(111) were shown to exhibit a higher activity but lower stability for CO_2 conversion compared with nearly stoichiometric $MoC_{1.1}$ NPs.[14] Thus, stoichiometry control serves as another lever for adjusting catalytic activity, comparable to the effect of bulk material surface orientation.[12] This is not surprising considering that carbon-vacancies on the bulk material surfaces can play a critical role, for example, in the RWGS catalyzed by VC.[22]

Departament de Ciència de Materials i Química Física & Institut de Química Teòrica i Computacional (IQTCUB), Universitat de Barcelona, c/Martí i Franquès 1-11, 08028 Barcelona, Spain. E-mail: francesc.illas@ub.edu

As for size effects, smaller clusters expose a larger fraction of low-coordinated active sites, with eased structural flexibility and, in general, higher reactivity, while larger particles offer greater thermodynamic stability due to lower formation energies per formula unit.[23] Furthermore, the catalytic activity of MoC_y clusters can be modulated by the support effect, where a diversity of materials has been used, including carbon-based materials,[20] zeolites,[24] and transition metals.[25] Among these, carbon-based materials have received increasing attention recently. For example, Liu *et al.* reported that MoC_y clusters on oxygen-enriched carbon nanotubes (CNT) exhibit superior RWGS rates and selectivities towards CO.[26] Additionally, MoC_y clusters anchored on a core@shell hybrid made of a nanodiamond@graphene (ND@G) structure were found to catalyze the RWGS with superior performance than MoC_y clusters supported by typical substrates such as γ-Al_2O_3.[27] Interestingly, Baddour *et al.*[20] observed that MoC_y clusters on a so-called inert carbon support exhibited a twofold increase in both activity and selectivity toward C_2 products compared to unsupported analogues. However, carbon support assumed passive *spectator* role is questionable, as its interaction with MoC_y clusters appears to significantly influence the overall catalytic performance.

In this context, graphene-based carbon materials have attracted considerable attention. Pristine flat graphene (FG) exhibits an inherently low chemical reactivity due to its fully conjugated sp^2-hybridized structure and highly aromatic stability. Thus, its potential effect has to be engineered, through *e.g.* surface modifications, heteroatom doping, and/or mechanical strain, in order to disrupt its π-conjugation and generate reactive sites.[28–30] Another shell of catalytic activity control that has attracted much attention recently is the graphene surface curvature, which originates intrinsically from thermal fluctuations or local strain.[31] Nanoripples and curved graphene (CG) have often been linked to enhanced catalytic activity in the literature. For example, She *et al.*[32] demonstrated that the surface curvature of oxidized CNT influences the oxygen reduction activity through charge redistribution and eventual stress of the epoxy groups. Similarly, Co_3O_4 clusters confined within CNT nanochannels were shown to exhibit better performance in contaminant removal processes compared to the counterparts located on the outer surface.[33]

In a recent study by some of us,[34] how MoC_y clusters of different sizes and stoichiometries interact with graphene-based supports of varying curvatures was studied in detail. Non-stoichiometric Mo-rich MoC_y clusters with low-coordinated Mo atoms exhibited stronger binding to the explored carbon supports by the additional formation of Mo–C bonds, fostered by a bond compensation mechanism. Additionally, the support curvature was found to increase the adsorption strength of MoC_y clusters on concave surfaces, while decreasing it on convex surfaces, revealing a strong linear correlation of the adsorption energy with the surface curvature.

However, this previous study did not address how support curvature influences the chemical and catalytic behavior of MoC_y clusters. In this work, we investigate this effect in the context of CO_2 adsorption and activation, using density functional theory (DFT) to comparatively study CO_2 interaction with both isolated and carbon-supported MoC_y clusters. Using the Mo-rich Mo_6C_5 cluster as a case study, we find that the local Mo_3 trimer site binds to CO_2 most strongly. However, this site has the highest chemical activity and serves as the anchoring point to carbon supports. Consequently, other sites with a more stoichiometric-like behavior—having both Mo and C atoms—become the most active ones for CO_2. This indicates that the carbon support can mitigate the over-reactivity of Mo-rich clusters,[14] while simultaneously promoting CO_2 activation at other available sites. Additionally, we find that the convex curvature of the support enhances CO_2 adsorption, whereas concave regions favor CO_2 dissociation, thereby promoting CO_2 catalytic conversion. These insights into the structural and electronic roles of the carbon support provide guidelines for designing more efficient and tailored MoC_y/C catalysts.

2. Computational models and methods

A strong interaction with the support is a prerequisite for studying the support effect on catalysis. Among the various possible compositions of MoC_y clusters studied earlier in their interaction with CO_2,[23] non-stoichiometric Mo-rich Mo_6C_5 was selected having its largest interfacial charge transfer and strongest adsorption when supported on FG and CG models,[34] and so possibly the largest catalytic activity effect (see Fig. 1). The Mo_6C_5 isomers were selected from previous works,[23] and reoptimized, confirming the most stable structure to further study its interaction with CO_2 and carbon supports.

Regarding the carbon supports, the FG was modeled by a $c(8 \times 6)$ supercell consisting of 96 carbon atoms. The supercell dimensions are 17.1 Å along the armchair direction (*a*-axis) and 14.8 Å along the zigzag direction (*b*-axis). A vacuum spacing of 20 Å was introduced perpendicular to the graphene surface to minimize interactions between periodically repeated graphene sheets. To model realistic CGs, models where the FG was compressed along the *a*-axis were used, as this modeling method effectively captures curvature effects at an affordable computational cost.[34] In particular, two CG models with different degrees of curvature—corresponding to diameters of 1.42 and 2.08 nm—were used, and geometries for both convex and concave surfaces are provided (see Fig. 1).

The DFT calculations were carried out using the Vienna *ab initio* simulation package (VASP) code.[35] The Perdew–Burke–Ernzerhof (PBE) functional[36] was chosen to describe the exchange and correlation energy terms, demonstrated to be suitable for describing Mo-based carbides.[37] The DFT Kohn–Sham (KS) equations were solved self-consistently by expanding the valence electron wavefunctions in a plane-wave basis set with a kinetic energy cutoff of 415 eV, which has been proven to deliver energy convergence within the chemical accuracy of 0.04 eV. The interactions between core and valence electrons were treated using the projector augmented-wave (PAW) method,[38] as implemented in VASP by Kresse and Joubert.[39]

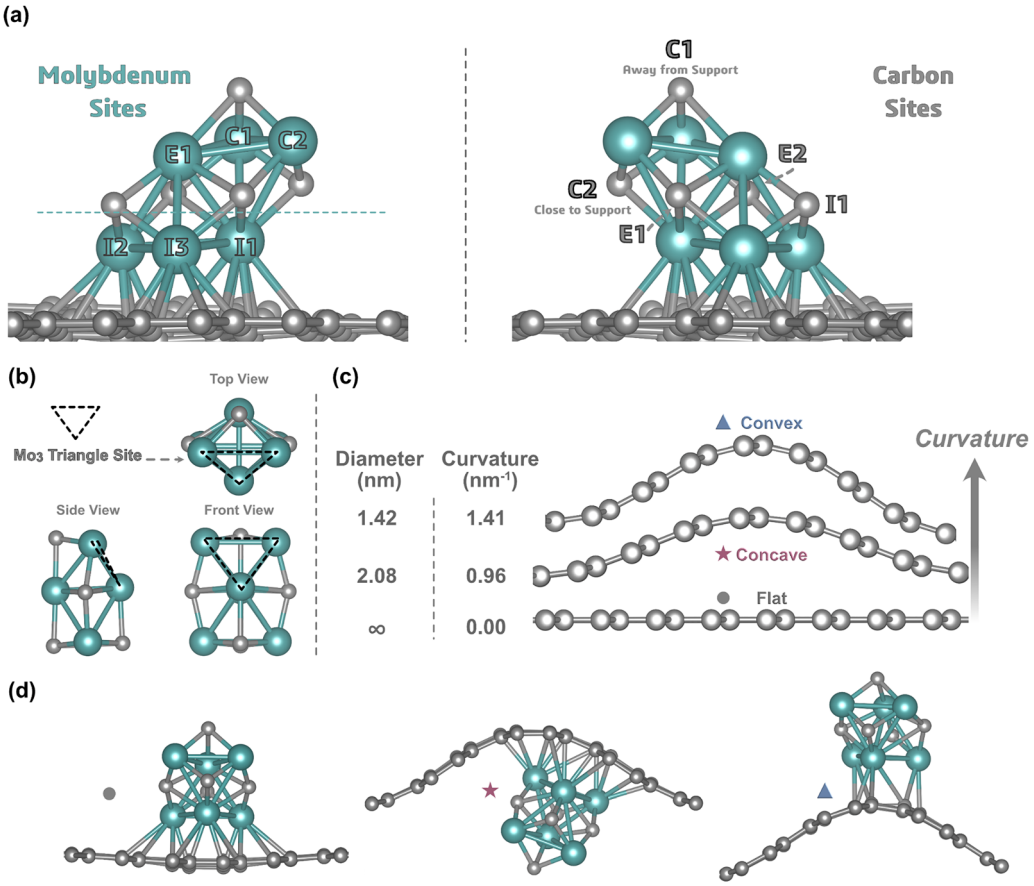

Fig. 1 Atomic representations of the Mo_6C_5/C models used in this work, including (a) active sites of the supported Mo_6C_5 cluster, involving edge (E), corner (C), and interface (I) sites; (b) the atomic structure of the Mo_6C_5 cluster in a vacuum, with the Mo_3 site tagged; (c) side views of FG and CG supports and corresponding diameters (in nm) and curvatures (in nm^{-1}), where an infinite diameter corresponds to graphene, with concave and convex sites tagged; and (d) side images of Mo_6C_5 on FG, convex and concave regions of CG. C and Mo atoms are represented by gray and cyan spheres, respectively.

Spin polarization tests—see Section S1 in the SI—indicate that spin polarization does not influence either the adsorption mode or the energetics of CO_2 on MoC_y/C catalysts, with variations below 0.01 eV, in line with earlier results.[14] Dispersive forces have been accounted for using Grimme's D3 approach.[40] The convergence thresholds for total energy and atomic forces were set to 10^{-5} eV and 0.01 eV $Å^{-1}$, respectively. For the chemical bonding analysis, Bader charges were calculated using the code developed by Henkelman *et al.*[41] For the isolated Mo_6C_5 and the CO_2 molecule in the gas phase, calculations were carried out by placing them in a large cubic box with 20 × 20 × 20 $Å^3$ dimensions, and calculations were at the **Γ** point only, required for non-periodic systems with no band dispersion. For Mo_6C_5 supported on the different carbon substrates, 3 × 3 × 1 Monkhorst–Pack **k**-points grids were employed, a choice validated by our **k**-point convergence test, as shown in Fig. S1 of the SI, ensuring energy convergence below chemical accuracy, *vide supra*.

The interaction strength of CO_2 on different Mo_6C_5/C models was quantified by first estimating the adsorption energy, E_{ads}. This energy was then decomposed into different contributions, including the deformation energy E_{def}, which describes the energy required to distort either the CO_2 molecule or the Mo_6C_5/C substrate from their respective optimized isolated structures to the configurations they adopt upon CO_2 adsorption, and the attachment energy, E_{att}, which accounts for the interaction energy between the deformed parts. Thus:

$$E_{ads} = E_{CO_2/subs} - E_{subs} - E_{CO_2} \quad (1)$$

$$E_{def} = E_X^{ads} - E_X^{free} \quad (2)$$

$$E_{att} = E_{ads} - E_{def}^{subs} - E_{def}^{CO_2} \quad (3)$$

where $E_{CO_2/subs}$ corresponds to the total energy of Mo_6C_5/C with CO_2 adsorbed; E_{subs} the total energy of the substrates (Mo_6C_5/C for supported cases, and Mo_6C_5 for isolated cases); E_{CO_2} the energy of the CO_2 molecule in the gas phase; and E_X^{ads} and E_X^{free} the total energy of a separated X entity (for substrates X is Mo_6C_5 or Mo_6C_5/C, for the adsorbate X is CO_2) in the adsorbed geometry and in its gas-phase optimized form, respectively. Finally, E_{def}^{subs} and $E_{def}^{CO_2}$ indicate the energy cost to deform Mo_6C_5/C (Mo_6C_5 for isolated cluster cases) and the CO_2 molecule, respectively. According to these definitions, the CO_2 adsorption is thermodynamically favorable when E_{ads} is negative, indicating an exothermic process. Likewise, a

negative E_{att} reflects a favorable interaction between the CO_2 and the catalyst; in contrast, E_{def} values are necessarily positive.

To describe the sites and bonding mode of CO_2 on the different models, we use a notation used in previous works[42] derived from coordination chemistry. For example, η^3-CO_2-μ^3-$C_BO_MO_M$ indicates the coordination of three atoms of the CO_2 molecule (η^3) with three atoms of the MoC_y cluster (μ^3), in such a way that the C atom of the CO_2 molecule is on a bridge site (C_B), either Mo–C, or Mo–Mo, while each of the CO_2 O atoms is located atop two metal atoms of the cluster (O_MO_M). Finally, to gather information on the chemical reactivity of the supported Mo_6C_5 cluster, the dissociation barrier of the adsorbed CO_2 into CO and O was evaluated by acquiring the transition state (TS) using the climbing-image nudged elastic band (CI-NEB) method,[43] with four intermediate images. The TS and minima were confirmed by vibrational frequency analysis, with TSs exhibiting a single imaginary frequency along the reaction coordinate. These vibrational frequencies were obtained by diagonalizing the appropriate block of the Hessian matrix, whose elements were computed as finite differences of analytical gradients, calculated only for the CO_2 molecule, *i.e.*, decoupled from substrate phonons.

3. Results and discussion

To facilitate the following discussion, we first present the results of CO_2 interacting with the bare Mo_6C_5 cluster, serving as a reference for the intrinsic adsorption behavior. Then, we examine the interaction of CO_2 with Mo_6C_5 supported on FG, which allows us to evaluate the effect of the carbon-based support. Finally, to reveal the effect of carbon support curvature, the CO_2 adsorption on Mo_6C_5 supported on CG models is presented.

3.1. CO_2 interaction with unsupported Mo_6C_5

The CO_2 interaction with the isolated Mo_6C_5 cluster in the gas phase was first evaluated considering all conceivable high-symmetry possible adsorption sites and modes. The E_{ads} values, shown in Fig. 2 and listed in Table 1, show that for bare Mo_6C_5, E_{ads} ranges from −0.83 to −2.68 eV. In particular, the strongest adsorptions, with E_{ads} of −2.01 and −2.68 eV, are both related to the Mo_3 hollow site (see Fig. 2), consistent with reported data.[23] This site would turn out to be inaccessible when the cluster is supported. However, the other sites that will still be available when Mo_6C_5 is adsorbed exhibit more moderate and reduced E_{ads} values from −0.83 to −1.55 eV. Clearly, local Mo-rich sites forming hollows are particularly active towards CO_2, as seen *e.g.* on similar two-dimensional Mo–carbides, the MXenes.[42] For the remaining sites (see Fig. 2), the strongest CO_2 adsorption is for the η^3-CO_2-μ^3-$C_CO_MO_M$ bonding mode with the CO_2 C atom on the topmost corner site, while the two CO_2 O atoms coordinate with seldom adjacent Mo atoms. Upon adsorption, a covalent C–C bond is generated with a length of 1.44 Å, falling within the typical range of C–C and C=C bond lengths. This CO_2 chemisorption leads to the symmetric elongation of both C–O bonds, with d(CO) from 1.17 Å in a vacuum to 1.34 Å in the adsorbed molecule (see Table 2). Simultaneously, the CO_2 bond angle, α(OCO), changes from 180° to 121.4°, with a charge transfer from MoC_y to CO_2 of 1.08e (see Table 1). Finally, even if such a conformation is not as strong as the adsorption on the Mo_3 site would be, it is still more pronounced than that on the δ-MoC (001) surface with E_{ads} of −1.35 eV,[18] highlighting the increased activity of the cluster compared to extended surfaces.

For most stable cases and other less strongly attached sites, the breakdown of the interaction energies is reported in Table 1 and visually shown in Fig. 3. In addition, the correlation between CO_2 adsorption and these energetic parameters, as well as relationships between the CO_2 Bader charge and α(OCO) with each of the four energy terms, are presented in Fig. S2 in the SI. Most relevant trends are shown in Fig. 3, revealing a linear trend between E_{ads} and the Bader charge (Q) of the adsorbed CO_2, thus underlining that stronger adsorption is accompanied by a larger electron transfer from the MoC_y cluster to the CO_2 molecule, reinforcing this charge transfer as the main driving force of CO_2 capture and activation.[44] Furthermore, an almost linear correlation is also found between the CO_2 angle, α(OCO), and the CO_2 deformation energy, implying that the energy cost of bending CO_2 is proportional to the acquired angle. So far, the interaction of CO_2 on the bare Mo_6C_5 has been fully described, and the question of the effect of flat graphene will be tackled next.

3.2. CO_2 interaction with Mo_6C_5 supported on FG

What would be the effect of the underlying FG support on the CO_2 interaction on an Mo_6C_5 cluster? To analyze this, it is first mandatory to understand the nature of the interaction between Mo_6C_5 and the FG substrate. As detailed in Section S1 of the SI, Mo_6C_5 interacts strongly with FG, with some electron transfer from the carbide cluster to the graphene, as detailed in a previous work.[34] In particular, the E_{ads} of Mo_6C_5 onto FG is as strong as −3.66 eV, which is almost 1 eV larger than the energy of the interaction of CO_2 on the Mo_6C_5 Mo_3 site (see Table 1 and Fig. 4), thus backing up the concept that such a site will be employed to anchor on the FG, and therefore, only other sites of the cluster will be available for CO_2. Having discarded the involvement of the Mo_3 site, all possible CO_2 adsorption configurations on the remaining sites are presented in Fig. 5, with detailed results shown in Tables 3 and 4, and a comparison of the different energy contributions is shown in Fig. 4, along with the isolated Mo_6C_5 reference. Preliminary tests confirmed that CO_2 weakly physisorbs onto pristine FG and CG supports (E_{ads} is approximately −0.4 eV), with no significant CO_2 activation, *i.e.*, negligible distortion of bond length and angle, in agreement with the literature for the interaction of CO_2 on carbon nanotubes.[45] Because this interaction is much weaker than that with the MoC_y, we focused our analysis on the composite system of MoC_y/C.

Upon supporting Mo_6C_5 on FG, note that the Mo_3 site anchors the cluster on FG, and Mo_6C_5 atoms are classified as

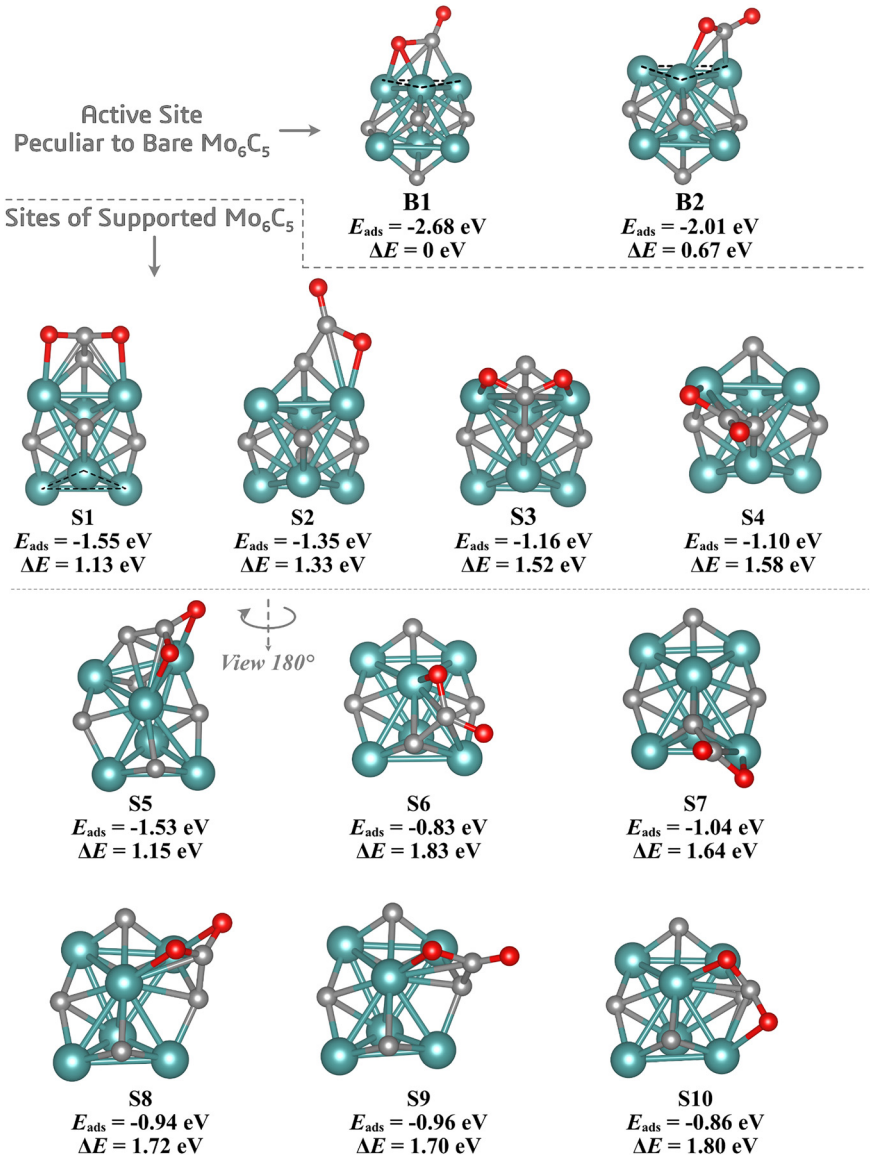

Fig. 2 Labelled atomic structures with adsorption energies, E_{ads}, and relative adsorption energies, ΔE, in eV, for CO_2 adsorbed on bare Mo_6C_5. Red spheres denote O atoms, while the rest of the color coding is as in Fig. 1.

Table 1 Results for CO_2 adsorption on isolated Mo_6C_5, including adsorption configurations, E_{ads}, E_{def}^{subs}, $E_{def}^{CO_2}$, and E_{att}, all in eV. Q corresponds to the Bader charge of the adsorbed CO_2, in e. E_{ads} of CO_2 on the extended δ-MoC (001) surface is included for comparison.[20] For CO_2 in the gas phase, d(CO) is calculated to be 1.18 Å and α(OCO) is 180°

Config.	E_{ads}	E_{def}^{subs}	$E_{def}^{CO_2}$	E_{att}	Q
B1	−2.68	0.39	3.50	−6.57	−1.51
B2	−2.01	0.39	2.02	−4.42	−1.24
S1	−1.55	0.93	3.63	−6.11	−1.08
S2	−1.35	0.64	3.11	−5.10	−0.76
S3	−1.16	0.40	2.84	−4.40	−0.88
S4	−1.10	0.46	2.95	−4.52	−0.76
S5	−1.53	0.88	3.56	−5.97	−1.11
S6	−0.83	0.45	2.96	−4.24	−0.88
S7	−1.04	0.33	2.92	−4.29	−0.74
S8	−0.94	0.32	2.90	−4.16	−0.88
S9	−0.96	0.24	2.80	−4.00	−0.73
S10	−0.86	0.48	3.10	−4.44	−0.96
δ-MoC (001)	−1.35	—	—	—	—

corner, edge, and interface sites, as shown in Fig. 1, with progressively higher coordination numbers. Notably, corner sites of Mo/C are more positively/negatively charged than other sites (see Fig. S3), enabling stronger interactions with CO_2, a point validated later. Additionally, a notable increase in the electronic states near the Fermi level, E_F, is observed (see the spin-polarized density of states (DOS) in Fig. S4 of the SI), which also includes the isolated Mo_6C_5 cluster and pristine FG. This can be an indication of enhanced electronic activity due to the interaction between the cluster and support. This is better appreciated in the differential DOS (see Fig. S4 of the SI) gained after subtracting the sum of the isolated components from the composite material, *i.e.*, Mo_6C_5 and FG. This resulting redistribution of electronic density provides direct evidence of electronic coupling and charge delocalization at the interface.

Table 2 Results for CO_2 adsorption on isolated Mo_6C_5, including the CO_2 adsorption bonding mode, bond lengths, d(CO), given in Å for each of the two bonds, and molecular angle, α(OCO), given in degrees. Values for the extended δ-MoC (001) surface are included for comparison.[18] For CO_2 in the gas phase, d(CO) is calculated to be 1.18 Å and α(OCO) is 180°

Config.	Bonding mode	d(CO)	d(CO)	α(OCO)
B1	η^2-CO_2-μ^3-$C_BO_MO_M$	1.42	1.23	123.7
B2	η^2-CO_2-μ^2-C_CO_M	1.29	1.26	134.1
S1	η^3-CO_2-μ^3-$C_BO_MO_M$	1.34	1.34	121.4
S2	η^2-CO_2-μ^2-C_CO_M	1.38	1.22	124.7
S3	η^3-CO_2-μ^3-$C_BO_MO_M$	1.30	1.30	125.8
S4	η^2-CO_2-μ^2-C_CO_M	1.37	1.22	125.5
S5	η^3-CO_2-μ^3-$C_BO_MO_M$	1.35	1.33	122.9
S6	η^3-CO_2-μ^3-$C_BO_MO_M$	1.32	1.29	125.1
S7	η^2-CO_2-μ^2-C_CO_M	1.36	1.22	125.4
S8	η^3-CO_2-μ^3-$C_BO_MO_M$	1.31	1.30	125.6
S9	η^2-CO_2-μ^2-C_CO_M	1.35	1.22	126.0
S10	η^3-CO_2-μ^3-$C_BO_MO_M$	1.31	1.31	124.3
δ-MoC (001)	η^1-CO_2-μ^1-C_C	1.29	1.29	129.0

Another general trend observed is that the presence of the FG support enhances CO_2 adsorption, particularly on most attachment sites, as seen in Fig. 4, where in a series of cases, CO_2 binds more strongly to the Mo_6C_5/FG than to the unsupported Mo_6C_5, *i.e.*, with more negative E_{ads} values. In particular, the enhancement is more remarkable on the first four sites, S1 to S4, belonging to the four lowest-coordinated atoms (see Fig. 1), *i.e.*, corner Mo atoms, and corner C atoms either far from or close to the support. These four atoms form a quadrilateral region that exhibits significantly stronger CO_2 adsorption than other sites. On average, the E_{ads} of sites S1 to S4 increase by approximately 0.58 eV compared with the corresponding sites on the unsupported Mo_6C_5 cluster.

As far as the coordination effect is concerned, it is worth stating that the S1 and S3 configurations adopt the η^3-CO_2-μ^3-$C_CO_MO_M$ binding mode. A clear tip effect is observed, also present in the bare cluster: CO_2 binds farthest from the carbon support, as in configuration S1, with stronger adsorption (~0.36 eV) than at the carbon site closer to the support, as in configuration S3. Furthermore, S1 shows stronger adsorption than configuration S2, highlighting that the η^3-CO_2-μ^3-$C_CO_MO_M$ mode is more favorable than the η^2-CO_2-μ^2-C_CO_M mode, having three contact points instead of two, in line with trends observed on the unsupported cluster. Notably, by comparing configurations S1 and S5 on Mo_6C_5/FG, both featuring the same binding mode, it can be seen that the substitution of one corner Mo with an edge Mo (see Fig. 5) results in a significant weakening of CO_2 adsorption, with E_{ads} reduced by ~0.78 eV. However, the same comparison on the bare Mo_6C_5 cluster shows only a negligible difference of ~0.02 eV. This suggests that the carbon substrate polarizes the electronic structure of Mo_6C_5, enhancing the reactivity of interface and tip sites while suppressing the activity of middle-region sites toward CO_2 activation. Following this logic, the observed

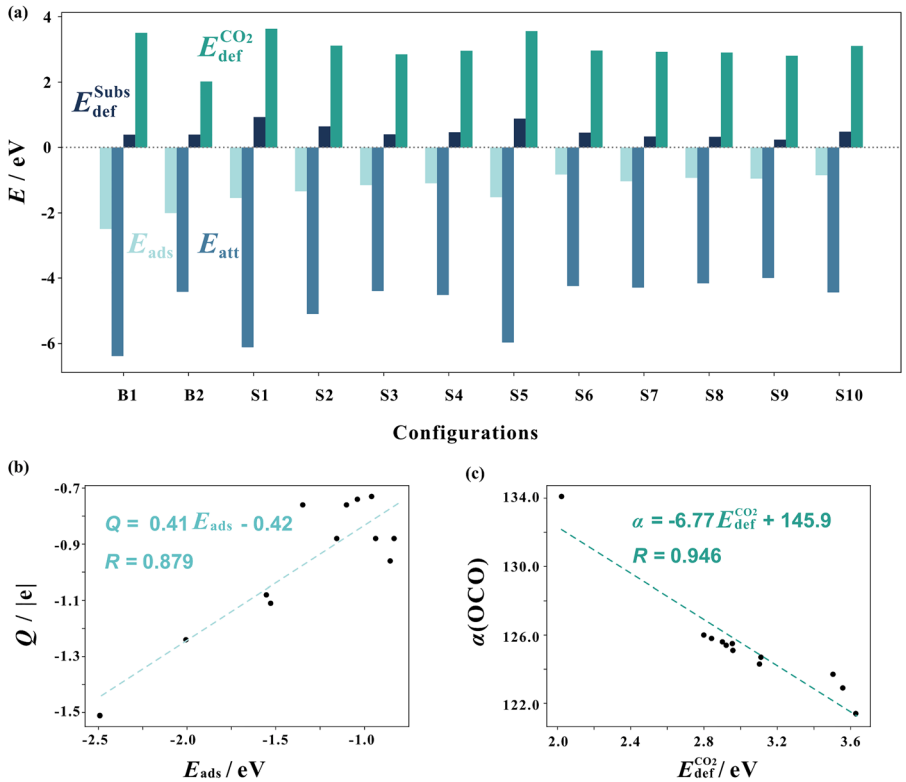

Fig. 3 (a) CO_2 adsorption on bare Mo_6C_5 on the different sites and modes and the energy contribution breakdown; (b) Bader charge (Q) of adsorbed CO_2 *vs.* E_{ads}, showing the linear correlation and the regression coefficient, R; and (c) α(OCO) *vs.* the deformation energy of CO_2, with the linear equation and R value.

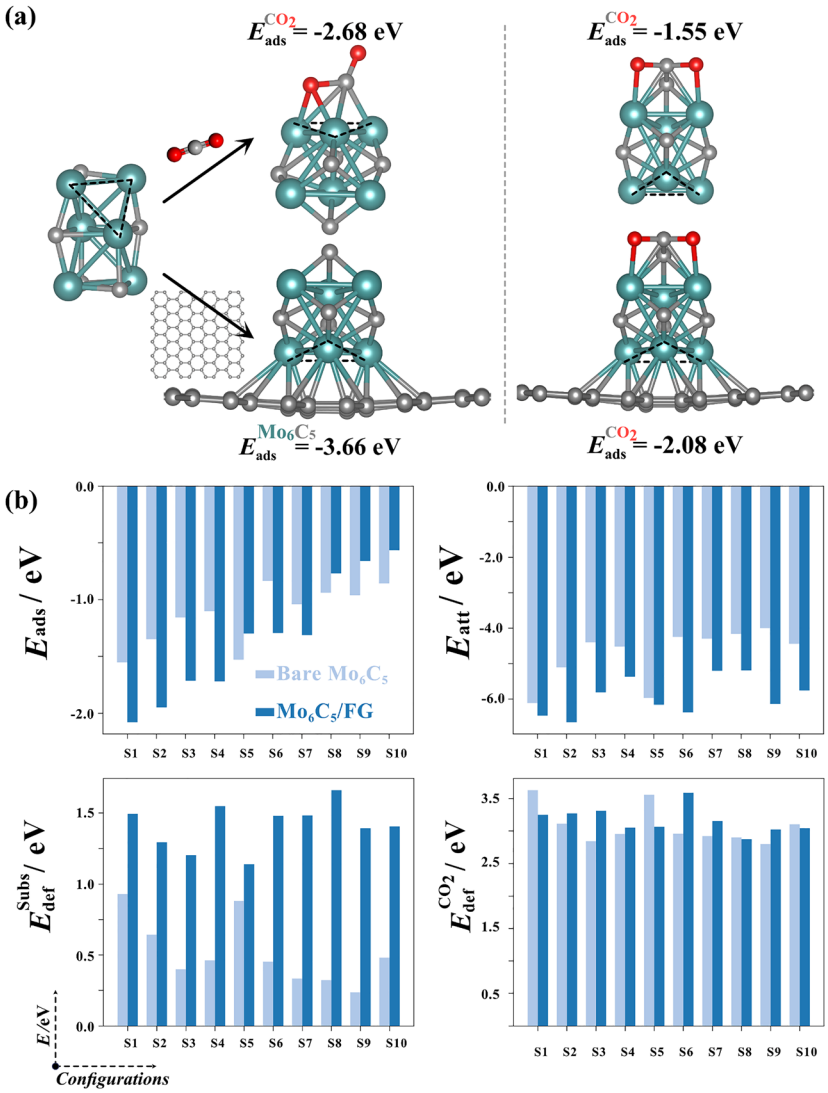

Fig. 4 (a) Left: The most stable CO_2 adsorption on bare Mo_6C_5 (top) and the most stable Mo_6C_5 adsorption on FG with corresponding E_{ads} values. Right: The most favorable CO_2 adsorption on Mo_6C_5/FG (bottom) and the corresponding site on bare Mo_6C_5 (top). The atom colors are as in Fig. 2. (b) Comparison of adsorption energetics for ten configurations on bare Mo_6C_5 and Mo_6C_5/FG.

decrease of E_{ads} for configurations S8 to S10 on Mo_6C_5/FG relative to the bare cluster case can be reasonably attributed to the involvement of middle-region sites (see the Mo and C edge sites in Fig. 1).

Interestingly, it appears that for all CO_2 adsorption configurations on Mo_6C_5/FG, the E_{def}^{subs} values are significantly higher than those of the bare cluster (see the energy contributions in Fig. 4). To understand the structural difference between supported and bare clusters, we analyzed the geometrical root-mean-square displacement (RMSD) values for all studied configurations reported in see Table S1. Taking the CO_2 adsorption configuration S1 as a reference, the RMSD of bare Mo_6C_5 decreases from 0.15 Å to 0.09 Å upon support on FG. This, together with the higher deformation energy of the Mo_6C_5/FG composite and the smaller distortion of the cluster, highlights the significant deformation occurring in the graphene support. Although the RMSD of the support is modest ($\sim$0.013 Å, see Table S1), the large number of carbon atoms (96) confirms its intrinsic flexibility.

This analysis supports a kind of support-mediated fluxional mechanism, where the redistribution of strain contributes to both enhanced stability and improved catalytic performance, without compromising the integrity of the cluster's active sites. As the carbon support undergoes significant structural relaxation in response to CO_2 adsorption on the supported cluster, the correlation between E_{ads} and the Bader charge is weakened, as shown in Fig. S5 of the SI. Instead, as shown in Fig. S6, another clear correlation emerges between the deformation energy of the CO_2 molecule and its Bader charge, Q. Regarding the CO_2 deformation energy, no consistent trend is observed upon adsorption at the FG-supported Mo_6C_5 (see Fig. 4). The extent of CO_2 bending varies depending on specific adsorption configurations. However, due to the markedly larger deformation energies of the support, the calculated E_{att} values are

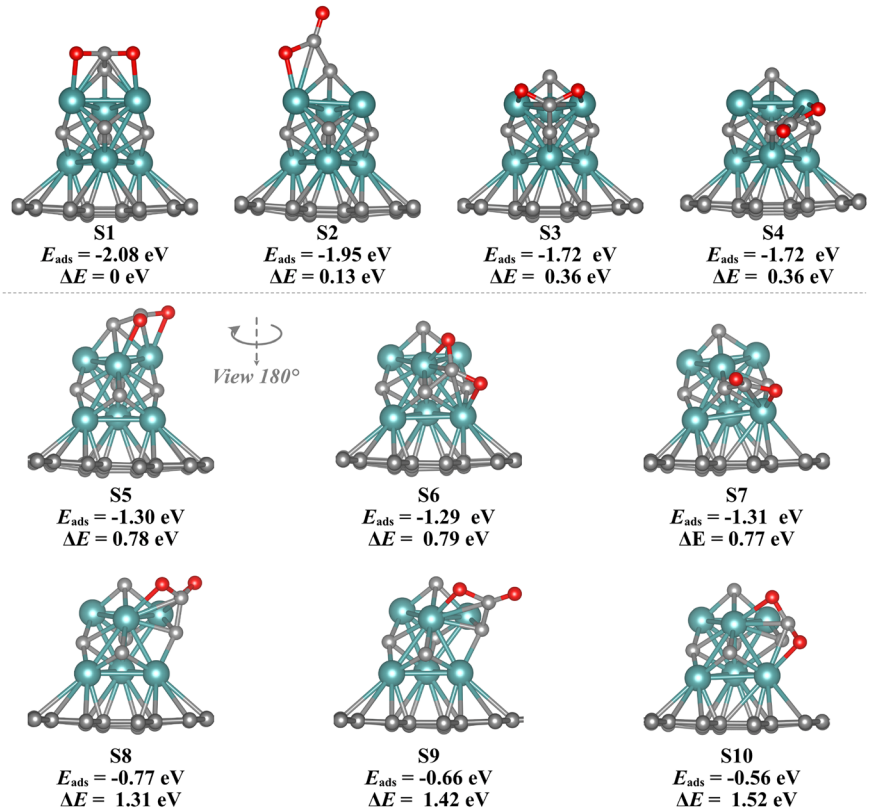

Fig. 5 Side view of adsorbed CO_2 structures on Mo_6C_5/FG, with E_{ads} and ΔE values. The color coding is as in Fig. 2.

Table 3 CO_2 adsorption on Mo_6C_5 on FG, including adsorption configuration, E_{ads}, E_{def}^{subs}, $E_{def}^{CO_2}$, and E_{att}, all in eV. Q corresponds to the Bader charge of the adsorbed CO_2, in e

Config.	E_{ads}	E_{def}^{subs}	$E_{def}^{CO_2}$	E_{att}	Q
S1	−2.08	1.29	3.27	−6.64	−0.95
S2	−1.95	1.14	3.06	−6.15	−0.76
S3	−1.72	1.49	3.25	−6.46	−1.01
S4	−1.72	1.39	3.02	−6.14	−0.78
S5	−1.30	1.48	3.59	−6.37	−1.08
S6	−1.29	1.20	3.31	−5.81	−0.95
S7	−1.31	1.40	3.04	−6.14	−0.74
S8	−0.77	1.55	3.05	−5.37	−0.91
S9	−0.66	1.66	2.87	−5.19	−0.70
S10	−0.56	1.48	3.15	−5.20	−0.97

Table 4 Results for CO_2 adsorption on Mo_6C_5 on FG, including the CO_2 adsorption bond sites, lengths, d(CO), given in Å for each of the two bonds, and molecular angle, α(OCO), given in degrees

Config.	Bonding mode	d(CO)	d(CO)	α(OCO)
S1	η^3-CO_2-μ^3-$C_BO_MO_M$	−2.08	1.32	1.32
S2	η^2-CO_2-μ^2-C_CO_M	−1.95	1.38	1.22
S3	η^3-CO_2-μ^3-$C_BO_MO_M$	−1.72	1.32	1.32
S4	η^2-CO_2-μ^2-C_CO_M	−1.72	1.38	1.22
S5	η^3-CO_2-μ^3-$C_BO_MO_M$	−1.30	1.33	1.35
S6	η^3-CO_2-μ^3-$C_BO_MO_M$	−1.29	1.31	1.33
S7	η^2-CO_2-μ^2-C_CO_M	−1.31	1.37	1.22
S8	η^3-CO_2-μ^3-$C_BO_MO_M$	−0.77	1.32	1.31
S9	η^2-CO_2-μ^2-C_CO_M	−0.66	1.35	1.22
S10	η^3-CO_2-μ^3-$C_BO_MO_M$	−0.56	1.30	1.32

generally more negative for Mo_6C_5/FG than for the bare clusters across all configurations (see Fig. 4). This indicates that, despite the additional structural cost from deformation, the overall attachment between CO_2 and the supported cluster is thermodynamically more favorable than on the bare cluster.

3.3. CO_2 interaction with Mo_6C_5 supported on CG surfaces

Finally, the introduction of substrate curvature may further affect the electronic properties of the supported metal carbide, and, in turn, affect its chemistry. This is clear from the adsorption energy of the Mo_6C_5 cluster on concave and convex regions of CG. For a given curvature (κ = 1.41 nm^{-1}, see Fig. S7 of the SI), Mo_6C_5 binds more strongly on the concave region of the support than on FG, with an enhanced adsorption of the Mo_6C_5 from −3.66 eV to −3.94 eV. This is accompanied by a larger electron transfer from the carbide to the substrate, 1.85e *vs.* 1.66e for FG, as estimated from Bader analysis of the electron density. In contrast, for the same curvature, the interaction in convex regions is weaker (E_{ads} of −2.87 eV), with a reduced charge transfer (1.50e). This trend is consistent with previous findings, where a concave surface enhances carbide–carbon support interaction and charge redistribution, while the opposite occurs for convex regions.[34] Furthermore, even if the Mo_6C_5 cluster displays a discrete spectrum of energy levels, we

found it convenient to consider the equivalent of the d-band center of Mo_6C_5 on FG, which is shown in Fig. S8. The d-band center shifts from −0.96 eV for support on FG to −0.83 and −0.58 eV when supported in the concave and convex regions,

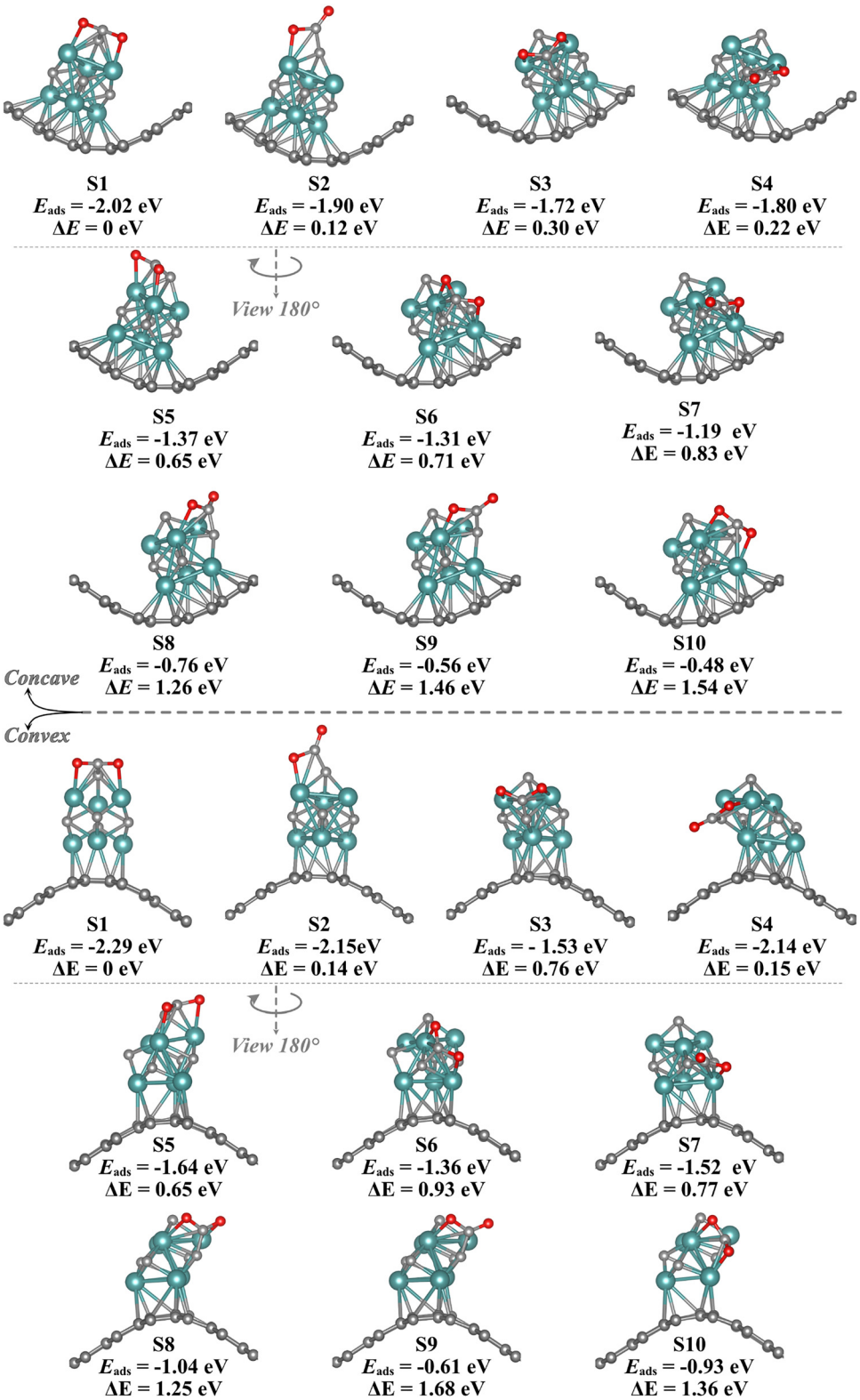

Fig. 6 Structures for CO_2 adsorption in concave regions (top) and convex regions (bottom) of Mo_6C_5/CG, with E_{ads} and ΔE values. The color coding is as in Fig. 2.

respectively. This modulation of the d-band center by substrate curvature partly governs the different activities toward CO_2 adsorption and activation, as discussed in the following parts.

To further analyze the effect of curvature of the C support on the Mo_6C_5/CG model systems, all possible CO_2 adsorption configurations on Mo_6C_5 supported on both concave and convex regions of CG were systematically explored, as illustrated in Fig. 6. The configuration indices were kept consistent with those used in bare and FG-supported cases to facilitate direct comparison. Detailed energetics and structural information can be found in Fig. S9, S10 and Tables S2, S3 in the SI. In Fig. 7, the CO_2 adsorption energies for Mo_6C_5 supported on carbon substrates with concave and convex geometries are systematically compared across all configurations.

Regardless of whether the Mo_6C_5 cluster is supported in concave or convex regions, configuration S1 remains the most stable available site for CO_2 adsorption. For this binding mode, the CO_2 adsorption strength follows the order convex > FG > concave, with E_{ads} values of −2.29 eV, −2.08 eV, and −2.02 eV, respectively (see Fig. 7). This indicates that the local curvature modulates the carbide–support interaction and, consequently, the CO_2 adsorption strength. Convex-supported Mo_6C_5 exhibits the strongest adsorption and thus the most favorable activation potential. For all S1 configurations, CO_2 adsorption on carbon-supported Mo_6C_5 is consistently stronger than on the bare cluster; even the weakest case on the concave-supported surface still outperforms the corresponding site on bare Mo_6C_5 (−1.55 eV), highlighting the overall promotional effect of the carbon support. These results underline that, in addition to MoC_y stoichiometry and surface sites, substrate curvature is another tuning parameter for MoC_y chemical activity.

Next, we briefly discuss the rest of the CO_2 adsorption configurations. Across all curvatures, S2 follows the trend already observed for S1, with binding of CO_2 on the topmost active sites with the η^2-CO_2-μ^2-C_CO_M binding mode having generally weaker bonds than the η^3-CO_2-μ^3-$C_CO_MO_M$ mode. Interestingly, a comparison between S1 and S3 on both concave and convex surfaces reveals that the sites farther from substrate exhibit stronger CO_2 activation capacity compared to closer sites, once again confirming the already mentioned tip effect as identified above in bare and FG-supported Mo_6C_5 systems. To further elucidate this behavior from an electronic structure perspective, the projected DOS (PDOS) for the two distinct carbon atoms was computed, having Mo_6C_5/FG as a reference (see Fig. S11 of the SI). The PDOS analysis shows that these farther sites exhibit a higher DOS near the E_F level compared to closer sites. This suggests a larger availability of electronic states for interaction with CO_2, which likely facilitates stronger adsorption and activation at these sites. Statistical analysis in Fig. 7 shows that nine out of ten CO_2 adsorption configurations on Mo_6C_5 supported in convex regions exhibit more negative adsorption energies than in concave regions, indicating

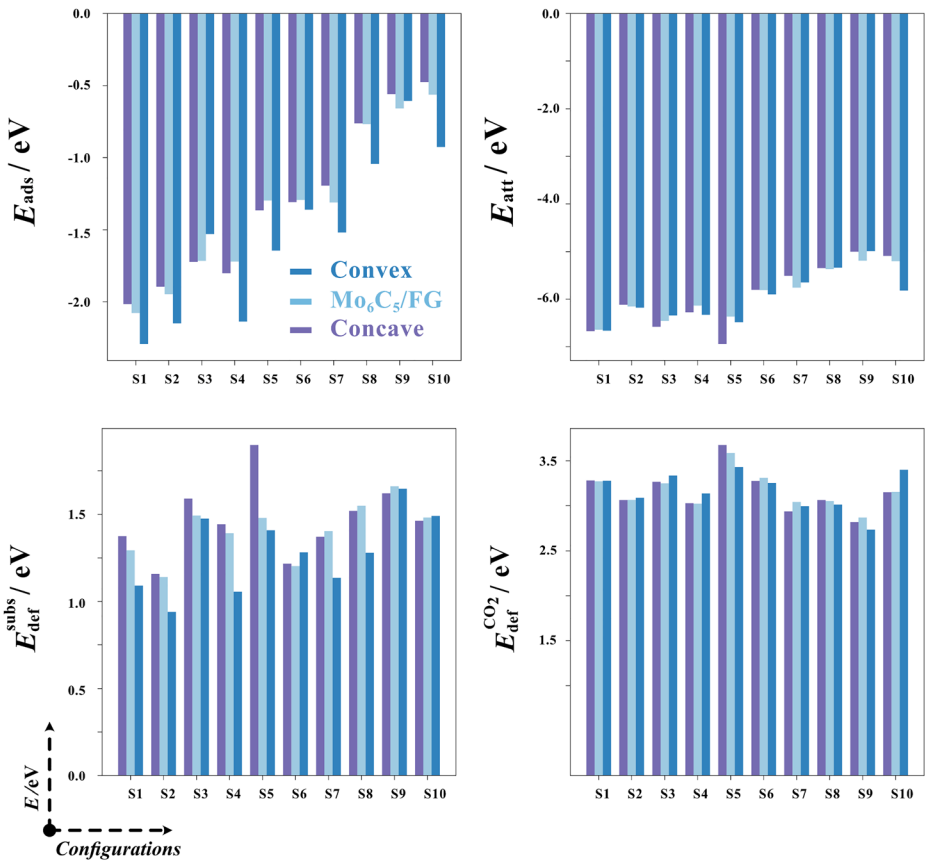

Fig. 7 Adsorption energy breakdown contributions of CO_2 on Mo_6C_5 clusters supported by FG and CG.

generally stronger CO_2 adsorption on convex-supported systems. In contrast, no clear trend is observed in the deformation energies of CO_2 molecules between the two curvature types. However, within each case, CO_2 deformation energies correlate well with the Bader charges, Q, of the adsorbed molecule and the α(OCO) angle bending, as shown in Fig. S9 and S10 of the SI. Regarding substrate deformation, configurations on concave surfaces typically exhibit larger deformation energies, likely due to the stronger carbide–support interaction in these regions, an effect that ultimately results in weaker E_{ads} but comparable E_{att} across both curvatures.

3.4. CO_2 dissociation on Mo_6C_5 supported on CG surfaces

To further investigate the effect of the carbon support on the chemistry of the supported Mo_6C_5 cluster, we explored the CO_2 dissociation pathway on Mo_6C_5 supported on FG and on the concave and convex regions of CG. For consistency, the most stable adsorption configuration S1 mode is used for all systems. The corresponding total energy profile is shown in Fig. 8 with the corresponding energy barriers, E_b, and reaction step energy changes, ΔE, summarized in Table S4 of the SI.

Compared to the bare Mo_6C_5 cluster, which shows an E_b of 1.72 eV, all supported cases exhibit significantly lower barriers ($\sim$1.10 eV), confirming the promoting effect of carbon supports. The concave CG-supported system presents the lowest E_b and most favorable ΔE, indicating enhanced CO_2 activation and conversion in concave regions. Although the energy barrier difference between convex and concave regions is modest ($\sim$0.07 eV), it accounts for approximately 6.7% of the overall energy barrier, which may translate into a significantly amplified effect on reaction kinetics due to the exponential dependence of the rate on the activation energy barrier, as described by standard transition state theory (TST):

$$k = \frac{k_B T}{h} \frac{Q^{\#}}{Q^{react}} e^{-\frac{E_b}{k_B T}}, \quad (4)$$

where k is the reaction rate, $Q^{\#}$ and Q^{react} are the partition functions at the transition state and reactant configurations, respectively, k_B is the Boltzmann constant, h is Planck's constant, and T is the reaction temperature. To estimate the kinetic impact of a 0.07 eV difference in the activation barrier between convex and concave configurations, a rough estimate can be obtained by simply assuming that the $\frac{k_B T}{h} \frac{Q^{\#}}{Q^{react}}$ preexponential factor is approximately the same for the reaction at concave and convex regions. Therefore, at room temperature, one would get:

$$\frac{k_{concave}}{k_{convex}} = \exp\left(\frac{E_{concave} - E_{convex}}{RT}\right) = \exp\left(\frac{0.07 \times 96.485}{8.314 \times 300}\right) \approx 15,$$

indicating that the modest difference in E_b implies a 15-fold increase in the reaction rate, underscoring the so far unknown but significant role of support curvature in tuning the catalytic activity of supported MoC_y clusters toward CO_2 conversion.

To conclude the analysis, we computed the vibrational frequencies of CO_2 adsorbed on Mo_6C_5 for the S1 configuration as a representative example across the above systems, with results summarized in Table S5 of the SI. The results show that the vibrational frequencies of adsorbed CO_2 are significantly different from those of the gas phase molecule. However, the values for the adsorbed molecule vary by less than 10 cm^{-1} across the different surface curvatures, indicating that such small differences may be challenging to resolve experimentally *via* infrared spectroscopy. The similarity in vibrational signatures suggests that the nature of the CO_2 binding remains essentially the same across the different support geometries. Therefore, the observed differences in CO_2 adsorption energies are attributed primarily to the influence of the carbon support on the electronic properties of the Mo_6C_5, as discussed in previous work.[34]

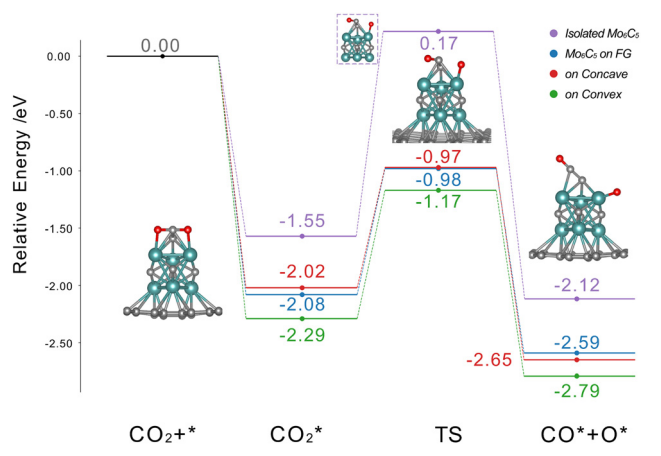

Fig. 8 CO_2 dissociation energy profiles on bare Mo_6C_5 clusters and on FG, concave CG, and convex CG surface models.

4. Conclusions

The interaction of CO_2 with bare and carbon-supported Mo_6C_5 clusters, taken as an example, has been systematically studied using DFT calculations with the PBE-D3 functional. On bare Mo_6C_5, the highly reactive Mo_3 site strongly binds and activates CO_2. When supported on flat graphene, the carbon support coordinates with this locally metal-rich site, mitigating the potential overactivity and instability observed in previously reported Mo-rich MoC_y clusters,[14] and promoting the activity of remaining near-stoichiometric active sites toward CO_2 adsorption and activation. Introducing support curvature further modulates the interaction: the convex regions enhance CO_2 adsorption, while the Mo_6C_5 anchored in concave regions shows the lowest CO_2 dissociation energy barrier, with the most favorable exothermic ΔE, implying that the support curvature is another parameter for tuning the catalytic activity of supported MoC_y clusters. These findings are likely to be general and highlight the key, yet previously disregarded, role of carbon support curvature, guiding the future rational design of MoC_y/C catalysts with improved catalytic performance toward CO_2 conversion.

Conflicts of interest

There are no conflicts of interest to declare.

Data availability

Input and output files are available from the authors upon request.

Supplementary information: The supplementary information contains the **k**-point convergence test; linear correlations between the CO_2 Bader charge and the molecule angle *vs.* energy contribution breakdowns; atomic and electronic structure analysis of Mo_6C_5/FG; Density Of States (DOS) of supported Mo_6C_5; Root-Mean-Square Displacement (RMSD) of fragments in interactions; Projected DOS (PDOS) for *d*-orbitals of supported Mo_6C_5; tip effect of supported Mo_6C_5 towards CO_2 adsorption; table of energy profile of CO_2 adsorption and activation on supported Mo_6C_5; vibrational frequencies of CO_2 adsorbed on isolated and supported Mo_6C_5. See DOI: **https://doi.org/10.1039/d5cp02714d**.

Acknowledgements

The research carried out at the Universitat de Barcelona has been supported by the Spanish MCIN/AEI/10.13039/501100011033 PID2021-126076NB-I00 and TED2021-129506B-C22 projects, partially funded by FEDER Una manera de hacer Europa, and by the María de Maeztu CEX2021-001202-M grant. The authors acknowledge partial support from COST Action CA18234 and from the Generalitat de Catalunya 2021SGR79 grant. W. C. thanks the China Scholarship Council (CSC) for financing his PhD (CSC 202308440222). F. V. thanks the ICREA Academia Award 2023 with Ref. Ac2216561.

References

1 J. Ye, N. Dimitratos, L. M. Rossi, N. Thonemann, A. M. Beale and R. Wojcieszak, *Science*, 2025, **387**, eadn9388.
2 M. D. Porosoff, B. Yan and J. G. Chen, *Energy Environ. Sci.*, 2016, **9**, 62–73.
3 E. V. Kondratenko, G. Mul, J. Baltrusaitis, G. O. Larrazábal and J. Pérez-Ramírez, *Energy Environ. Sci.*, 2013, **6**, 3112–3135.
4 W. Wang, S. Wang, X. Ma and J. Gong, *Chem. Soc. Rev.*, 2011, **40**, 3703–3727.
5 D. Preti, C. Resta, S. Squarcialupi and G. Fachinetti, *Angew. Chem., Int. Ed.*, 2011, **50**, 12551–12554.
6 W. Bi, J. Wang, R. Zhang, Q. Ge and X. Zhu, *ACS Catal.*, 2024, **14**, 11205–11217.
7 A. M. Abdellah, F. Ismail, O. W. Siig, J. Yang, C. M. Andrei, L.-A. DiCecco, A. Rakhsha, K. E. Salem, K. Grandfield, N. Bassim, R. Black, G. Kastlunger, L. Soleymani and D. Higgins, *Nat. Commun.*, 2024, **15**, 938.
8 X. Jiang, X. Nie, X. Guo, C. Song and J. G. Chen, *Chem. Rev.*, 2020, **120**, 7984–8034.
9 J. A. Rodriguez, P. Liu, Y. Takahashi, K. Nakamura, F. Viñes and F. Illas, *Top. Catal.*, 2010, **53**, 393–402.
10 H. H. Hwu and J. G. Chen, *Chem. Rev.*, 2005, **105**, 185–212.
11 R. B. Levy and M. Boudart, *Science*, 1973, **181**, 547–549.
12 X. Liu, C. Kunkel, P. Ramirez de la Piscina, N. Homs, F. Viñes and F. Illas, *ACS Catal.*, 2017, **7**, 4323–4335.
13 H. Prats and M. Stamatakis, *J. Mater. Chem. A*, 2022, **10**, 1522–1534.
14 M. Figueras, R. A. Gutiérrez, F. Viñes, P. J. Ramírez, J. A. Rodriguez and F. Illas, *ACS Catal.*, 2021, **11**, 9679–9687.
15 M. A. Khoshooei, X. Wang, G. Vitale, F. Formalik, K. O. Kirlikovali, R. Q. Snurr, P. Pereira-Almao and O. K. Farha, *Science*, 2024, **384**, 540–546.
16 H. K. Lim, H. Shin, W. A. Goddard III, Y. J. Hwang, B. K. Min and H. Kim, *J. Am. Chem. Soc.*, 2014, **136**, 11355–11361.
17 H. Li and K. Reuter, *ACS Catal.*, 2020, **10**, 11814–11821.
18 S. Posada-Pérez, F. Viñes, P. J. Ramirez, A. B. Vidal, J. A. Rodriguez and F. Illas, *Phys. Chem. Chem. Phys.*, 2014, **16**, 14912–14921.
19 T. Wang, X. Liu, S. Wang, C. Huo, Y.-W. Li, J. Wang and H. Jiao, *J. Phys. Chem. C*, 2011, **115**, 22360–22368.
20 F. G. Baddour, E. J. Roberts, A. T. To, L. Wang, S. E. Habas, D. A. Ruddy, N. M. Bedford, J. Wright, C. P. Nash, J. A. Schaidle, R. L. Brutchey and N. Malmstadt, *J. Am. Chem. Soc.*, 2020, **142**, 1010–1019.
21 J. A. Rodriguez, C. Jimenez-Orozco, E. Flórez, F. Viñes and F. Illas, *J. Phys. Chem. C*, 2023, **127**, 16764–16780.
22 A. Pajares, H. Prats, A. Romero, F. Viñes, P. Ramírez de la Piscina, R. Sayós, N. Homs and F. Illas, *Appl. Catal., B*, 2020, **267**, 118719.
23 C. Jimenez-Orozco, M. Figueras, E. Flórez, F. Viñes, J. A. Rodriguez and F. Illas, *Phys. Chem. Chem. Phys.*, 2022, **24**, 16556–16565.
24 J. Gao, Y. Zheng, G. B. Fitzgerald, J. De Joannis, Y. Tang, I. E. Wachs and S. G. Podkolzin, *Phys. Chem. Chem. Phys.*, 2014, **16**, 4670–4679.
25 J. M. Horn, Z. Song, D. V. Potapenko, J. Hrbek and M. G. White, *J. Phys. Chem. B*, 2005, **109**, 44–47.
26 S. Cao, Z. Guan, Y. Ma, B. Xu, J. Ma, W. Chu, R. Zhang, G. Giambastiani and Y. Liu, *ACS Catal.*, 2024, **14**, 10939–10950.
27 S. Cao, Y. Ma, W. Chu and Y. Liu, *Fuel*, 2022, **323**, 124347.
28 M. B. Burkholder, F. B. A. Rahman, E. H. Chandler Jr, J. R. Regalbuto, B. F. Gupton and J. M. M. Tengco, *Carbon Trends*, 2022, **9**, 100196.
29 R. J. Koch, M. Weser, W. Zhao, F. Viñes, K. Gotterbarm, S. M. Kozlov, O. Höfert, M. Ostler, C. Papp, J. Gebhardt, H.-P. Steinrück, A. Görling and T. Seyller, *Phys. Rev. B:Condens. Matter Mater. Phys.*, 2012, **86**, 075401.
30 M. Surana, G. Ananthakrishnan, M. M. Poss, J. J. Yaacoub, K. Zhang, T. Ahmed, N. C. Admal, P. Pochet, H. T. Johnson and S. Tawfick, *Nano Lett.*, 2023, **23**, 1659–1665.
31 P. Xu, M. Neek-Amal, S. D. Barber, J. K. Schoelz, M. L. Ackerman, P. M. Thibado, A. Sadeghi and F. M. Peeters, *Nat. Commun.*, 2014, **5**, 3720.

32 F. She, Z. Guo, F. Liu, Z. Yu, J. Chen, Y. Fan, Y. Lei, Y. Chen, H. Li and L. Wei, *ACS Catal.*, 2024, **14**, 10928–10938.
33 T. Liu, S. Xiao, N. Li, J. Chen, X. Zhou, Y. Qian, C.-H. Huang and Y. Zhang, *Nat. Commun.*, 2023, **14**, 2881.
34 W. Cao, M. Figueras-Valls, F. Viñes and F. Illas, *ACS Appl. Mater. Interfaces*, 2025, **17**, 7098–8108.
35 G. Kresse and J. Furthmüller, *Phys. Rev. B:Condens. Matter Mater. Phys.*, 1996, **54**, 11169.
36 J. P. Perdew, K. Burke and M. Ernzerhof, *Phys. Rev. Lett.*, 1996, **77**, 3865.
37 J. R. dos Santos Politi, F. Viñes, J. A. Rodriguez and F. Illas, *Phys. Chem. Chem. Phys.*, 2013, **15**, 12617–12625.
38 P. E. Blöchl, *Phys. Rev. B:Condens. Matter Mater. Phys.*, 1994, **50**, 17953.
39 G. Kresse and D. Joubert, *Phys. Rev. B:Condens. Matter Mater. Phys.*, 1999, **59**, 1758.
40 S. Grimme, J. Antony, S. Ehrlich and H. Krieg, *J. Chem. Phys.*, 2010, **132**, 154104.
41 W. Tang, E. Sanville and G. Henkelman, *J. Phys.: Condens. Matter*, 2009, **21**, 084204.
42 Á. Morales-García, A. Fernández-Fernández, F. Viñes and F. Illas, *J. Mater. Chem. A*, 2018, **6**, 3381–3385.
43 G. Henkelman and H. Jónsson, *J. Chem. Phys.*, 2000, **113**, 9901–9904.
44 C. Kunkel, F. Viñes and F. Illas, *Energy Environ. Sci.*, 2016, **9**, 141–144.
45 D. Quinonero, A. Frontera and P. M. Deya, *J. Phys. Chem. C*, 2012, **116**, 21083–21092.